

See discussions, stats, and author profiles for this publication at: <https://www.researchgate.net/publication/340665878>

# The Mountain Weather and Climate of Denali, Alaska – An Overview

Article in *Journal of Applied Meteorology and Climatology* · April 2020

DOI: 10.1175/JAMC-D-19-0105.1

CITATION

1

READS

168

2 authors, including:



[Lea Hartl](#)

Austrian Academy of Sciences (OeAW)

37 PUBLICATIONS 130 CITATIONS

[SEE PROFILE](#)

Some of the authors of this publication are also working on these related projects:



pluSnow – Using snow depth data to minimize the error in winter precipitation measurements [View project](#)



Denali (AK) weather and climate [View project](#)

# The Mountain Weather and Climate of Denali, Alaska—An Overview

LEA HARTL AND MARTIN STUEFER

*Alaska Climate Research Center, Geophysical Institute, University of Alaska Fairbanks, Fairbanks, Alaska*

TOHRU SAITO

*International Arctic Research Center, University of Alaska Fairbanks, Fairbanks, Alaska*

(Manuscript received 6 May 2019, in final form 6 December 2019)

## ABSTRACT


An overview of climatological and meteorological conditions and their seasonal variability in the Denali summit region is presented, based on the NCEP–NCAR reanalysis 1 dataset for the 1948–2018 period. At the Denali grid cell, a warming trend of  $+0.02^{\circ}\text{C}$  significant at the 95% level is found—equivalent to a temperature increase of  $1.4^{\circ}\text{C}$  over the time period. The number of very cold days ( $<-35^{\circ}\text{C}$ ) during the climbing season (April–July) has decreased by approximately a day per decade. The number of very windy days ( $\geq 20\text{ m s}^{-1}$ ) during the climbing season also shows a decreasing trend for the majority of the time series. To assess synoptic patterns that affect the Denali region, a self-organizing map algorithm was applied to the geopotential height (GPH) field extracted from the reanalysis data. In winter, the synoptic situation in the Denali region is dominated by frequent zonal flow and negative GPH anomalies associated with the polar front. As the polar front moves north during the seasonal cycle, patterns shift to largely positive GPH anomalies and more meridional flow. Extreme wind speeds unfavorable for climbing occur in all seasons and are associated mainly with the polar jet passing directly over Denali, or cyclogenesis in the Bering Sea. The frequency of occurrence of strongly zonal, low GPH patterns during the main climbing season (April–July) shows a slight decrease in recent years.


## 1. Introduction

With a summit elevation of 6190 m above sea level (MSL) and a topographic prominence of 6144 m, Denali—formerly known as Mount McKinley—is the world’s third most prominent and third most isolated mountain. Since the early twentieth century, it has attracted climbers hoping to reach the summit of the highest mountain of the Alaska Range and the North American continent. The number of climbers on Denali rose rapidly from the 1960s to about 1990, when numbers stabilized at around 1100 climbers per season (Denali National Park Service 2018). Due to its geographic isolation and the large

elevation difference between base and summit, Denali significantly affects atmospheric flow at the micro and mesoscale and is known to “create its own weather,” which is characterized by high wind speeds and cold temperatures and is hence often unfavorable for mountaineering activities. Medical search and rescue calls on Denali are frequently related to the cold environment. Avalanche danger—another key threat to climbers—is also driven by meteorological conditions (McIntosh et al. 2010, 2012). Extreme wind gusts are thought to have played a role in a number of climbing falls. In one fatal incident, “clues suggested that high winds blew the climber off the mountain” (McIntosh et al. 2008).

On the scale of global atmospheric circulation, much of Denali’s often unfavorable climbing weather can be attributed to its latitude. At  $63^{\circ}\text{N}$ , Denali lies within the influence of the polar jet stream and the polar front and associated storm tracks. In the fall and winter months, the atmospheric circulation upstream of Denali is characterized by low pressure systems, which tend to develop in the northwestern Pacific due to temperature gradients between cold continental air masses and warmer,

 Denotes content that is immediately available upon publication as open access.

 Supplemental information related to this paper is available at the Journals Online website: <https://doi.org/10.1175/JAMC-D-19-0105.s1>.

Corresponding author: Lea Hartl, [lbhartl@alaska.edu](mailto:lbhartl@alaska.edu)

DOI: 10.1175/JAMC-D-19-0105.1

© 2020 American Meteorological Society. For information regarding reuse of this content and general copyright information, consult the AMS Copyright Policy ([www.ametsoc.org/PUBSReuseLicenses](http://www.ametsoc.org/PUBSReuseLicenses)).

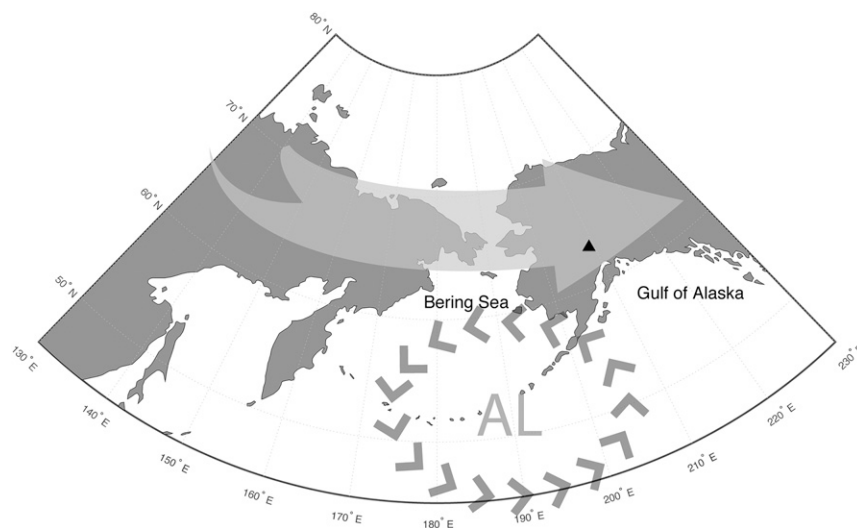


FIG. 1. Schematic depiction of a typical wintertime polar jet passing over Denali (black triangle). AL denotes the approximate position of the Aleutian low, a semipermanent center of low sea level pressure that forms near the Aleutian Islands.

maritime air (e.g., [Businger and Reed 1989](#)). Typically, low pressure centers tend to reach their maximum intensity near the Aleutian Islands to form a semipermanent area of low sea level pressure known as the Aleutian low (e.g., [Serreze et al. 1997](#); [Rodionov et al. 2005a, 2007](#); [Sun and Tan 2013](#)). Storm tracks following the polar front as well as the depth and position of the Aleutian low vary significantly on both interannual and decadal time scales ([Overland et al. 1999](#); [Rodionov et al. 2005b](#); [Pickart et al. 2009](#); [Sugimoto and Hanawa 2009](#); [Zhu et al. 2007](#); [Wang et al. 2012](#)). See [Fig. 1](#) for a schematic depiction of Denali in relation to the Aleutian low and the polar jet.

Sea salt sodium records in ice core data from Mount Hunter in the Alaska Range and Mount Logan in Canada show a strengthening of the Aleutian low since the eighteenth century ([Osterberg et al. 2017](#)). The Mount Hunter ice core also indicates that precipitation at the site has increased strongly since ~1840, potentially supporting the idea of increased storm activity associated with the Aleutian low ([Winski et al. 2017](#)). In contrast, for the past two decades, increased sea surface temperatures over the central North Pacific appear to correspond with a weakened Aleutian low and a more stable Arctic vortex ([Hu et al. 2018](#)).

Weather and overall climatic conditions as well as associated changes, trends, and variability clearly play an important role for mountaineering activities on Denali and the safety of the climbers. Yet, little is known about how specific synoptic-scale weather patterns in the North Pacific region effect conditions on the mountain. Regional Denali weather forecasting is

challenging due to the extreme environment, overall data sparsity, and comparatively poor model resolution of existing operational numerical weather forecast models.

As a first step toward addressing these issues and focusing specifically on the main climbing season (April–July), we discuss the following questions based on the NCEP–NCAR reanalysis 1 dataset:

- 1) How do key meteorological parameters such as wind, temperature, and geopotential height vary on Denali throughout the year and the main climbing season and how are they changing over time?
- 2) Can typical weather patterns, their seasonality, their variability during the climbing season, and their potential long-term trends be delineated and quantified based on reanalysis data?
- 3) Are there specific synoptic weather patterns, for example, with a preferred area of cyclogenesis, that are particularly hazardous to climbers and has this changed over time?

The paper is organized as follows: In [section 2](#), we give details on the data and methods [self-organizing map (SOM) analysis, Mann–Kendall trend testing] used. The first part of the results section ([section 3](#)) gives an overview of wind and temperature at the Denali grid cell and how these parameters vary throughout the year and the months of the climbing season. In the second part of the results section, the SOM analysis is presented, showing synoptic-scale weather patterns in and upstream of the Denali region, their seasonality, as well as patterns associated with high- and low-wind conditions

on the mountain. This is followed by a discussion of limitations and broader context (section 4), and concluding remarks (section 5).

## 2. Data and methods

### a. NCEP–NCAR reanalysis

The analysis of synoptic-scale weather patterns relevant to the Denali area is based on the NCEP–NCAR reanalysis 1 dataset (Kalnay et al. 1996). Those data are available globally on a grid of  $2.5^\circ$  latitude by  $2.5^\circ$  longitude from 1 January 1948 to present, for different levels of geopotential height, 4 times per day. Reanalysis data for the 1948–2018 period were obtained from NOAA/OAR/ESRL Physical Science Division, Boulder, Colorado, from their website (<https://www.esrl.noaa.gov/psd/>).

Geopotential height (GPH), air temperature, and  $u$  and  $v$  wind components at the 500 hPa level were extracted for the reanalysis grid cell that contains Denali to create time series of GPH, temperature, wind speed, and direction. Mean GPH at the 500 hPa level varies between 5222 m in December and 5627 m in July. Six-hourly data were resampled to daily values by extracting the maximum wind speed of the day and the associated wind direction, and by computing the arithmetic mean for temperature and GPH. Based on these values, a climatological overview of wind and temperature at the Denali grid cell was created.

### b. Self-organizing map algorithm

In addition to the analysis of wind and temperature parameters in the Denali grid cell in the reanalysis data at the 500 hPa level, regional synoptic patterns were assessed. To this end, a subset of the 500 hPa GPH grid data over the North Pacific was extracted from the global grid. The corners of the subset are at  $45^\circ\text{N}$ ,  $80^\circ\text{N}$ ,  $130^\circ\text{E}$ , and  $230^\circ\text{E}$ . To show areas of relative high and low GPH in and upstream of the Denali region, GPH anomalies were computed: For each reanalysis time step, the GPH value of each grid cell within the regional subset was subtracted from the mean over the global domain at that time (e.g., Cassano and Cassano 2010). Note that this shows areas of relative high and low pressure compared to the global mean at each individual time step, rather than gridpoint deviations from the climatological mean.

A SOM algorithm was used to identify recurring synoptic patterns in the 500 hPa GPH anomalies over the spatial subset extracted from the global reanalysis grid. The SOM is a type of unsupervised neural network commonly used to visualize and identify patterns

in complex, multidimensional datasets (Kohonen 2001). The SOM algorithm places nodes within the data space of an  $N$ -dimensional cloud of input data, such that the distribution of the nodes represents the distribution function of the input data. More nodes are placed in regions with high data density and similar nodes are located closer together, while dissimilar nodes are located farther apart in the final output map. The SOM assumes the input data to be continuous and, unlike other clustering techniques, the SOM does not make assumptions about the distribution of the data or the resulting clusters. The number of nodes is selected by the user depending on the size of the dataset and the desired application. The smaller the number of nodes, the broader the generalization by which subsets of the input data are clustered. A higher number of nodes will result in a finer level of detail in the output SOM, but will still show the same overall patterns (Hewitson and Crane 2002; Cassano et al. 2006). The algorithm detects the node most closely matching the presented input data [the best-matching unit (bmu)], as well as neighboring nodes within a certain radius of distance. The bmu as well as the neighboring units are then updated to more closely resemble the input data. As this process is repeated iteratively, the nodes of the SOM become characteristic of the input data space. The weight vectors of the nodes are of the same dimension as the input data vectors, that is, in our case the output nodes can be displayed in the style of synoptic maps in the same way as the input GPH anomalies. This allows for intuitive visualization and interpretation of the SOM nodes in terms of synoptic-scale GPH patterns in our region of interest (Hewitson and Crane 2002).

Using the entire dataset to train the SOM, the input GPH grids for each time step in the reanalysis data were then compared to the final SOM nodes by computing the Euclidean distance between the input grid and each node. The node for which the Euclidean distance is smallest represents the clustered pattern each input grid is mapped to and this yields a list of the time steps each node represents, which allows for further analysis related to the frequency and seasonal distribution of synoptic patterns as identified by the SOM (e.g., Cassano and Cassano 2010; Hewitson and Crane 2002). We used a  $7 \times 5$  SOM for an overview of the range of synoptic patterns that occur throughout the year, and a smaller  $3 \times 2$  SOM to obtain a broader clustering of typical patterns during the months of the main climbing season (April–July), and for both high- and low-wind days. Both SOMs were initialized with nodes randomly distributed within the input data space and trained sequentially. Our implementation of the SOM algorithm is based on the freely available SOM toolbox software package for MATLAB; details can be found

TABLE 1. Maximum, median, and standard deviation of wind speed, as well as the mean number of days (percentage of days) per month with daily wind maximum above  $20 \text{ m s}^{-1}$  and below  $10 \text{ m s}^{-1}$ , respectively, 1948–2018, Denali grid cell, 500 hPa level. Main climbing season highlighted in bold.

Month	Jan	Feb	Mar	Apr	May	Jun	Jul	Aug	Sep	Oct	Nov	Dec
Max ( $\text{m s}^{-1}$ )	51.6	51.5	49.4	<b>44.5</b>	<b>38.3</b>	<b>34.5</b>	<b>31.6</b>	38.6	45.9	44.5	52.9	54.2
Median ( $\text{m s}^{-1}$ )	13.4	13.3	11.9	<b>10.7</b>	<b>9.5</b>	<b>8.5</b>	<b>8.2</b>	9.6	10	10.5	11.4	12.8
Std dev ( $\text{m s}^{-1}$ )	8.5	8.2	7.6	<b>7.3</b>	<b>5.9</b>	<b>5.1</b>	<b>4.9</b>	6.2	7	6.7	7.8	8.2
Days over $20 \text{ m s}^{-1}$	11.9 (38%)	10.2 (36%)	8.6 (28%)	<b>7 (23%)</b>	<b>4.1 (13%)</b>	<b>2 (7%)</b>	<b>1.7 (5%)</b>	4.4 (14%)	6.3 (21%)	6.3 (20%)	8 (27%)	10.5 (34%)
Days under $10 \text{ m s}^{-1}$	5.5 (18%)	5 (18%)	7.1 (23%)	<b>9.2 (31%)</b>	<b>11.6 (37%)</b>	<b>14.1 (47%)</b>	<b>15 (48%)</b>	11.4 (37%)	10.2 (34%)	9.2 (30%)	6.9 (23%)	5.6 (18%)

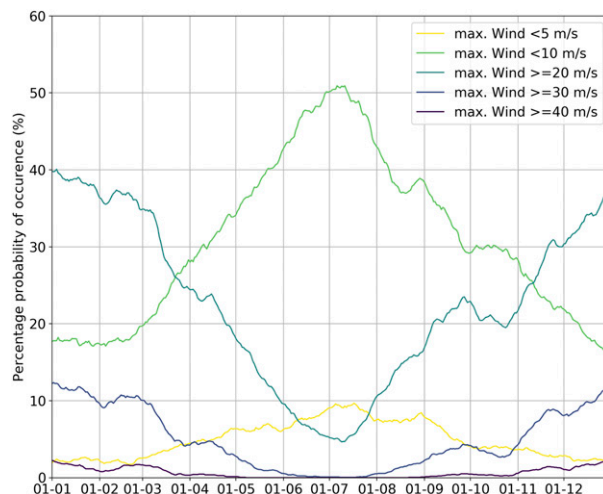


FIG. 2. Probability for wind speed above or below threshold values given in legend for each day of the year at the Denali grid cell, 500 hPa level, based on the 1948–2018 reanalysis dataset. Daily data were smoothed with a centered 15 day running mean.

in Vesanto et al. (1999) and the extensive documentation online (<http://www.cis.hut.fi/somtoolbox/>).

Reviews of SOM applications in meteorological and climatological studies can be found in Liu and Weisberg (2011) and Sheridan and Lee (2011). In-depth theoretical background can be found in Kohonen (1989, 1990, 1991, 2001).

### c. Mann–Kendall trend testing

To detect potential changes in the reanalysis data for the Denali grid cell and the frequency of occurrence of specific weather patterns during the climbing season, linear, nonparametric Mann–Kendall trend testing (Mann 1945; Kendall 1955) was carried out on overlapping subperiods of the time series of climatological temperature and GPH anomalies, as well as the annual frequency of occurrence of specific SOM nodes. The minimum length of the subperiods tested for trends is 10 years, resulting in 1891 subperiods for the 1948–2018 reanalysis dataset. Subperiods are defined by the central year and the window width [for further details on this method see Olefs et al. (2010)]. Significance of monotonic long-term changes is tested at  $p = 0.05$  and only significant trends are given.

## 3. Results

### a. Reanalysis Denali grid cell

#### 1) WIND

Reanalysis data wind speed shows a pronounced seasonality (Table 1). Considering the 6-hourly reanalysis

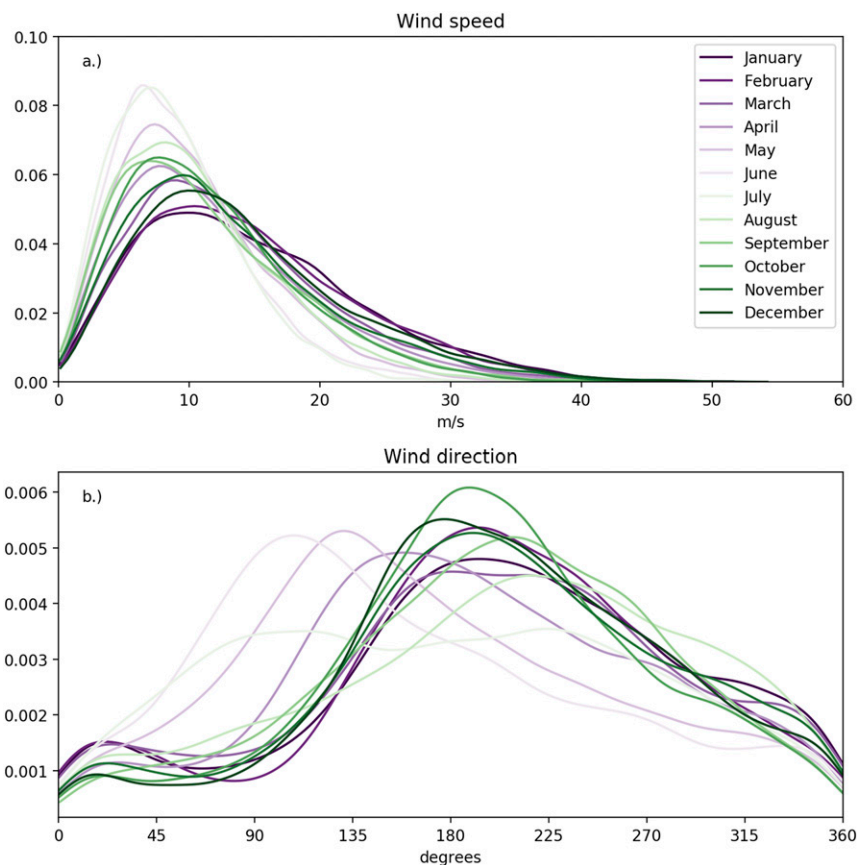


FIG. 3. Probability density functions estimated from histograms of (a) wind speed and (b) wind direction for the Denali grid cell at the 500 hPa level, grouped by month, 1948–2018.

data for 1948–2018, wind speeds greater than  $50 \text{ m s}^{-1}$  occur in November, December, January, and February. The absolute maximum wind speed for the reanalysis time series is  $54.2 \text{ m s}^{-1}$  (28 December 1951). The standard deviation of monthly wind speeds is highest in the winter months and lowest in June and July. June and July are the calmest months in terms of maximum and median wind speeds and have the highest number of days with wind speeds not exceeding  $10 \text{ m s}^{-1}$ .

Similarly, the percentage probability for wind speeds equal to or exceeding  $20 \text{ m s}^{-1}$  is below 10% for most of June and July, reaching the lowest values during the first half of July. The probability for wind speeds below  $10 \text{ m s}^{-1}$  inversely tracks the annual cycle of chances for winds above  $20 \text{ m s}^{-1}$ , reaching a maximum probability of just over 50% during the first half of July (Fig. 2). Chances for days with winds below  $5 \text{ m s}^{-1}$  are also highest in July, but they never exceed 10%. Overall, probabilities for winds above/below a particular threshold are fairly constant in January and February and see a sharp drop/rise from March until

early July, when the pattern is reversed. The mode of the monthly probability density functions for wind speed is shifted to lowest wind speeds and greatest frequency of occurrence in June and July and moves toward higher wind speeds and fewer occurrences in the spring, winter, and fall months (Fig. 3).

Wind direction also shows a seasonal cycle, though it is less pronounced than wind speed. In the winter months, winds mostly blow from the south and southwest and the highest wind speeds are associated with south and south-southwest winds. In April, May, and June, the dominant wind direction shifts toward the east, and the highest wind speeds are associated with south-southeast to east-southeast winds. In July, wind direction is more or less evenly distributed between west-southwest and east-southeast before it shifts back to predominantly southwest directions in August and throughout the fall season. Northerly winds are rare overall (Figs. 3 and 4).

During the main climbing season (April–July), wind speeds of  $20 \text{ m s}^{-1}$  or more occur on about 12% of days—taking into account the entire year, this value



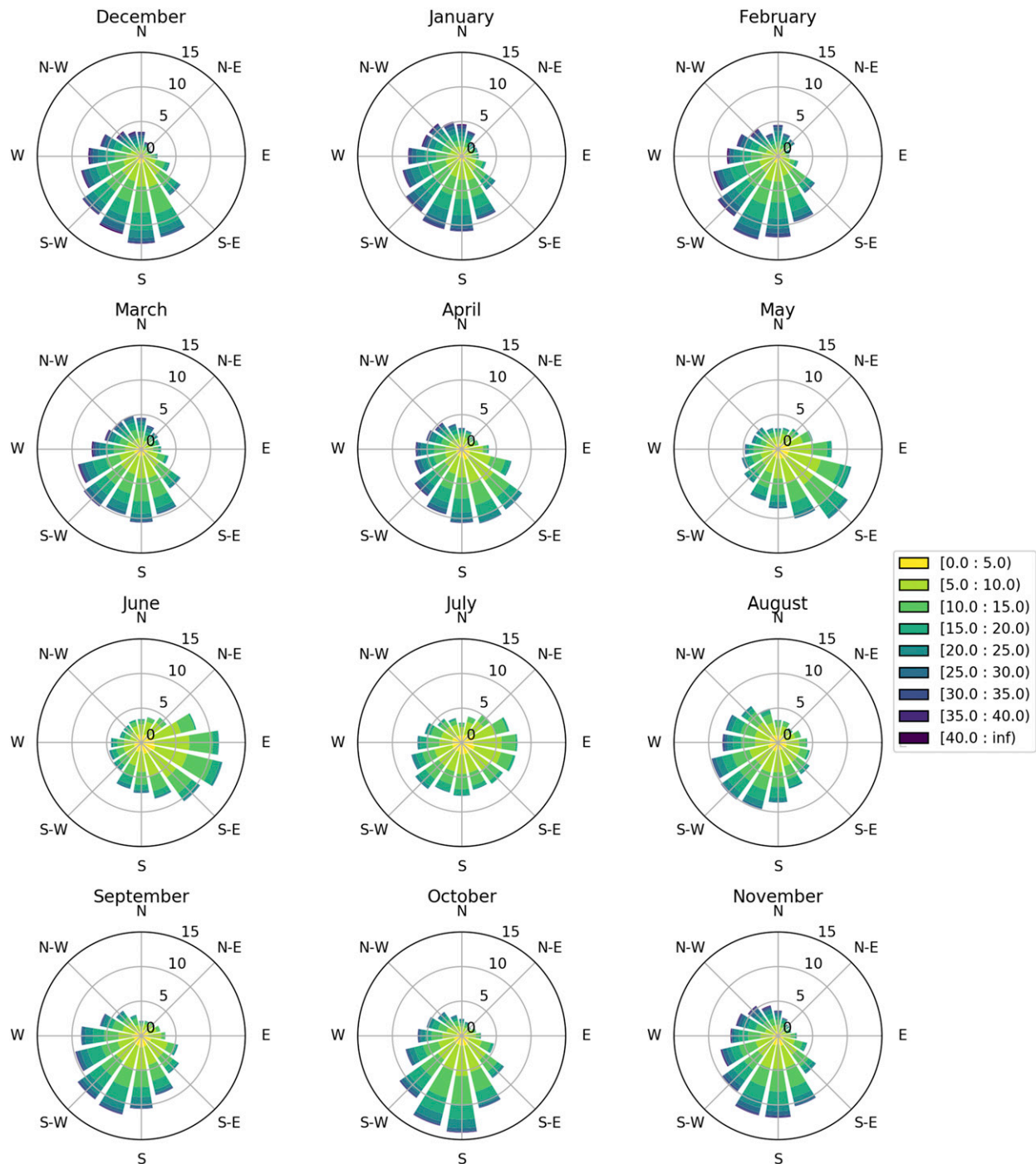


FIG. 4. Wind roses for the Denali grid cell at the 500 hPa level, grouped by month, 1948–2018. Colors indicate wind speed in  $\text{m s}^{-1}$ , frequency of occurrence of wind direction is plotted on the radial axis.

rises to 22% (Table 1). Mann–Kendall trend testing on the number of “windy days” (wind speed  $\geq 20 \text{ m s}^{-1}$ ) per climbing season shows a slight downward trend of approximately  $-0.1$  days per season for the 1957–2018 subperiod. This is the longest of a small number of

neighboring subperiods with trends of similar magnitudes. For the analogous time series of days with wind speed below  $10 \text{ m s}^{-1}$ , there are no long subperiods with significant trends and none that extend into recent years.

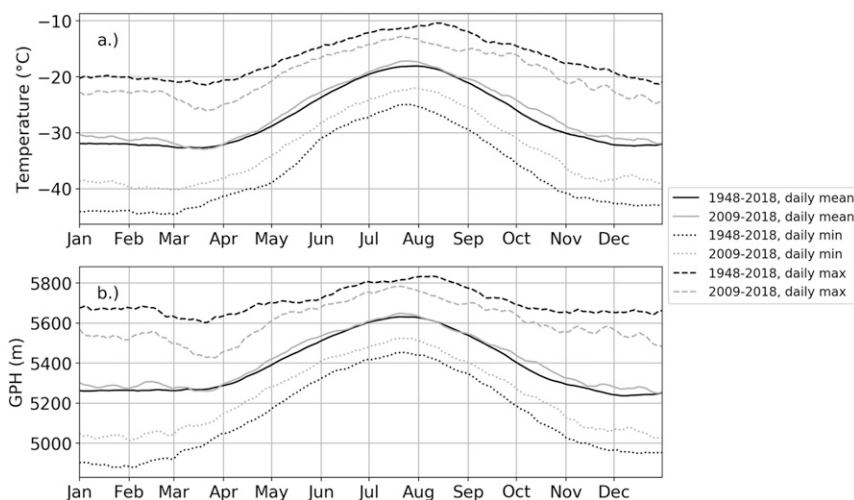


FIG. 5. Solid black lines show daily mean (a) air temperatures and (b) GPH averaged from 6 hourly values over the 1948–2018 period for the Denali grid cell at the 500 hPa level, as well as absolute daily highs (dashed) and lows (dotted). Gray lines show the same for the last 10 years of the dataset (i.e., 2009–18). Daily data were smoothed with a centered 15 day running mean.

## 2) TEMPERATURE AND GEOPOTENTIAL HEIGHT

The highest 500 hPa air temperature in the 1948–2018 6-hourly reanalysis time series was  $-7.4^{\circ}\text{C}$  on 24 August 1954. The lowest temperature was  $-49.2^{\circ}\text{C}$  on 17 February 1982. July and August are the warmest months and show the lowest standard deviation of temperature (Fig. 5, Table 2). From early December until the first half of March, temperatures are relatively constant at daily mean values of around  $-32^{\circ}\text{C}$ . In mid-March, temperatures begin increasing at a roughly constant rate until the summer maximum, which typically occurs in late July or early August. Temperatures then drop again until they reach the winter plateau in December (Fig. 5, Table 2).

Figure 5b shows daily GPH and air temperature values for an “average year,” that is, the mean value of each day of the year from 1948 to 2018, as well as the minimum and maximum values for that day. In addition to the curves for the entire time series, the data for the most recent decade (2009–18) are shown. Throughout most of the year and especially during the fall and winter months, mean air temperatures were higher in the last decade than averaged over the entire time series. Absolute daily minimum temperatures during the last decade were all several degrees higher than previous minimum values for the time series. Conversely, no new maximum values were reached during the 2009–18 period.

Figure 6a shows climatological temperature anomalies for the main climbing season (April–July). The 2004 season was exceptionally warm with an anomaly of  $3.6^{\circ}\text{C}$ —more than  $1.5^{\circ}\text{C}$  warmer than the two next

warmest years, 1991 and 2016. Nine of the 10 most recent years were warmer than the mean over the time series, as were 17 of the 20 last years. Figure 6b shows subperiods with trends significant at the 95% level. A large majority of significant trends is positive. The strongest warming trend ( $+0.26^{\circ}\text{C}$ ) occurs during a 10-yr period centered in the mid-1970s. This coincides with the 1976–77 phase change of the Pacific decadal oscillation (PDO) from negative to positive mode and the resulting shift toward a warmer climatic regime in Alaska (Hartmann and Wendler 2005; Marcus et al. 2011). For the entire time series, a significant warming trend of  $+0.02^{\circ}\text{C}$  is found—equivalent to a temperature increase of  $1.4^{\circ}\text{C}$  from 1948 to 2018. In general terms, the magnitude of warming trends decreases with the length of the respective subperiods and tends to increase for more recent subperiods. Averaged over the 1948–2018 period, there are approximately 10 days during the climbing season on which temperatures fall below  $-35^{\circ}\text{C}$ . The number of days below  $-35^{\circ}\text{C}$  has decreased by approximately a day per decade ( $-0.09$  days  $\text{year}^{-1}$ ) during this time period.

### b. Regional synoptic patterns

The 35 nodes of the  $7 \times 5$  SOM shown in Fig. 7 represent the distribution of GPH anomalies over the northern Pacific region for the 1948–2018 period. In the following we identify single nodes using a (row, column) notation. The percentages above the plots indicate the amount of input data mapped to the respective node. The position of each node within the SOM matrix is determined by how similar or dissimilar the nodes are,



TABLE 2. Maximum, minimum, mean, and standard deviation of air temperature, as well as the mean number of days (percentage of days) per month with minimum temperatures below  $-35^{\circ}\text{C}$ , respectively, 1948–2018, Denali grid cell, 500 hPa level. Main climbing season highlighted in bold.

Month	Jan	Feb	Mar	Apr	May	Jun	Jul	Aug	Sep	Oct	Nov	Dec
Max	-15.7	-14.6	-16.9	<b>-14.4</b>	<b>-11.3</b>	<b>-9.2</b>	<b>-8.7</b>	-7.4	-9.3	-10.1	-14.1	-14.3
Min	-48.5	-49.2	-48.8	<b>-44.5</b>	<b>-42.7</b>	<b>-33.3</b>	<b>-31.6</b>	-31.8	-39.5	-44.2	-45.5	-48.1
Mean	-31.8	-32.3	-32.8	<b>-31.1</b>	<b>-26.5</b>	<b>-21.5</b>	<b>-18.2</b>	-19	-23.6	-28.7	-31.4	-32.6
Std dev	5.6	5.5	5.1	<b>5</b>	<b>4.6</b>	<b>3.5</b>	<b>3.1</b>	3.9	4.4	5	5.4	5.5
Days under $-35^{\circ}\text{C}$	12.4 (40%)	12.4 (44%)	14.1 (45%)	<b>9.2 (31%)</b>	<b>1.2 (4%)</b>	<b>0 (0%)</b>	<b>0 (0%)</b>	0 (0%)	0.1 (0%)	3.8 (12%)	9.7 (32%)	14.1 (46%)

with similar nodes placed closer together. In the top-left corner of the matrix, a meridional flow pattern dominates the synoptic situation, with a shallow trough centered in the eastern Bering Sea and a pronounced ridge over Interior Alaska and the Denali region. GPH gradients are comparatively flat between the centers of high and low pressure within the domain and positive anomalies are predominant. Moving right in the matrix toward the top-right corner, nodes retain their meridional pattern defined by a trough in the west and a ridge in the east, but the trough deepens while the ridge becomes less pronounced. Gradients increase and negative anomalies become predominant. Moving down along the right side of the matrix, the flow pattern shifts to a zonal regime across the Bering Sea. In the node in the lower-right corner, the axis of a short-wave trough lies just west of Denali and extends into the Gulf of Alaska. This pattern is the most dissimilar to the meridional, low gradient pattern in the upper-left corner. Moving to the left side of the matrix along the lowest row, the overall zonal pattern is retained but anomalies shift to more positive values.

The nodes in the leftmost column of the matrix are largely associated with the summer season, with the maximum frequency of occurrence shifting from June for nodes (1, 1) and (2, 1) to July for (3, 1) and (4, 1), August for (5, 1) and (6, 1), and September for (7, 1). Moving right along the columns of the matrix, the maximum frequencies of the nodes shifts from summer to spring and fall (spring maxima are found mainly in the top half, fall months in the lower half of the matrix) and to the winter months for the rightmost column (Fig. 8). The node with the highest overall frequency of occurrence is (4, 1) and 9.1% of input data are mapped to this node. The neighboring nodes (3, 1) and (5, 1) also represent a comparatively large amount of input data points (6% and 5.1%, respectively). In the middle three columns, no node represents over 3% of input data. The nodes in the rightmost column represent between 3.6% and 5.9% of input data, with the exception of (2, 5), which occurs less often.

To provide a broader clustering of typical synoptic regimes for the climbing season, a  $3 \times 2$  SOM for April–July is shown in Fig. 9. The most frequent pattern overall (37.1% of input data) is node (1, 1) with a shallow, closed low over the Bering Sea and ridging over interior Alaska. This node occurs most often in July and is similar to the most frequent “summer nodes” in Fig. 7. Moving down and across the matrix from this “summer regime” at (1, 1), the maximum frequencies of occurrence of the nodes shift to earlier months. The second most frequent node

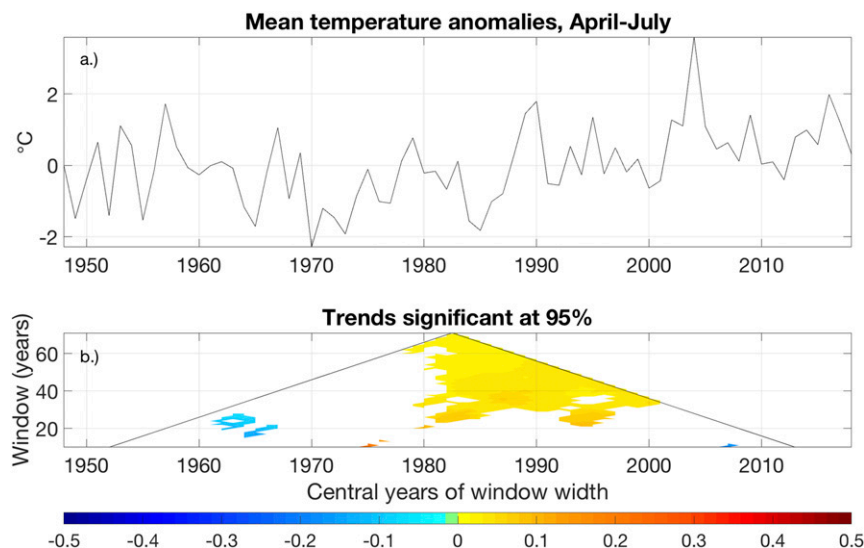


FIG. 6. (a) April–July air temperature deviations from the 1948–2018 mean, Denali grid cell, 500 hPa level. (b) Mann–Kendall trend analysis of all subperiods 10 years or longer. Subperiods are defined by the window width, or the length of the subperiod (y axis) and the central year of the period (x axis), that is, the top of the triangle represents the longest subperiod, spanning the entire 1948–2018 period. Colors represent the magnitude of the trends in °C per year, white areas represent subperiods with nonsignificant trends.

(31.5% of input data) is the most dissimilar, located at (3, 2) in the matrix, and resembles the most frequent “winter nodes” in Fig. 7 with a generally more zonal pattern, a western flow over the Bering Sea, and south to southwest flow over Denali. This node occurs most often in April, at the beginning of the climbing season. The frequency of occurrence of the nodes changes from year to year, with a standard deviation of 4%–5% for all nodes (Fig. 10).

The Mann–Kendall trend analysis of the frequency of node occurrence per climbing season for the 1948–2018 period indicates that node (3, 2) is occurring less often, more so in more recent subperiods, while node (1, 1) and (2, 2) are occurring more often. The longest subperiod with a significant trend for node (3, 2) is 1961–2017. The frequency of occurrence decreased by  $0.08\%$  season<sup>−1</sup> during this time. Shorter subperiods with decreasing trends extend to the end of the time series (2018). Conversely, the frequency of occurrence of node (1, 1) increased by  $0.08\%$  season<sup>−1</sup> from 1969 to 2016, that is, the longest subperiod with a significant trend for this node.

Figure 11 shows a  $3 \times 2$  SOM for days during the climbing season in which wind speed is  $20 \text{ m s}^{-1}$  or more. Large GPH gradients across the Denali area are characteristic of all nodes in this particular SOM. Again, the relatively small SOM size produces a generalized output identifying two dominant nodes, which are each associated with over 30% of the input data points, and 4

transitional nodes that fall between the patterns of the dominant nodes. Two main synoptic patterns produce high-wind conditions on Denali: The most frequent case [34.6% of input data mapped to node (1, 1)] is a “winter-type” pattern where the polar jet passes over Denali, producing a strong southwesterly flow downstream of a relatively low-amplitude trough. The trough axis is roughly on a longitude with the Kamchatka Peninsula and has a positive tilt. On the opposite end of the node spectrum [32% of input data mapped to node (3, 2)], Denali lies under a southerly flow with a slight easterly component. This is associated with a closed low centered in the Bering Sea, just southwest of Saint Lawrence Island, and a pronounced ridge east of Denali. In this case, the trough axis connecting the closed low to the large-scale circulation has a negative tilt, as does the axis of the ridging pattern downstream of the trough. This pattern is a variation of the main summer nodes of Figs. 9 and 11 but GPH anomaly gradients are notably more pronounced. Nodes (1, 1) and (2, 1) of Fig. 11 occur primarily in April. Nodes (3, 1) and (1, 2) occur most often in April and May. Node (2, 2) occurs in May in over 50% of instances. Node (3, 2) occurs in May, June, and July, and almost never in April. The overall number of days with wind speeds of  $20 \text{ m s}^{-1}$  or more shows a decreasing trend [see section 3a(1)]. Applying the Mann–Kendall trend test to the different nodes representing the synoptic patterns on these days during the climbing season, node (1, 1)—the most frequent winter-type

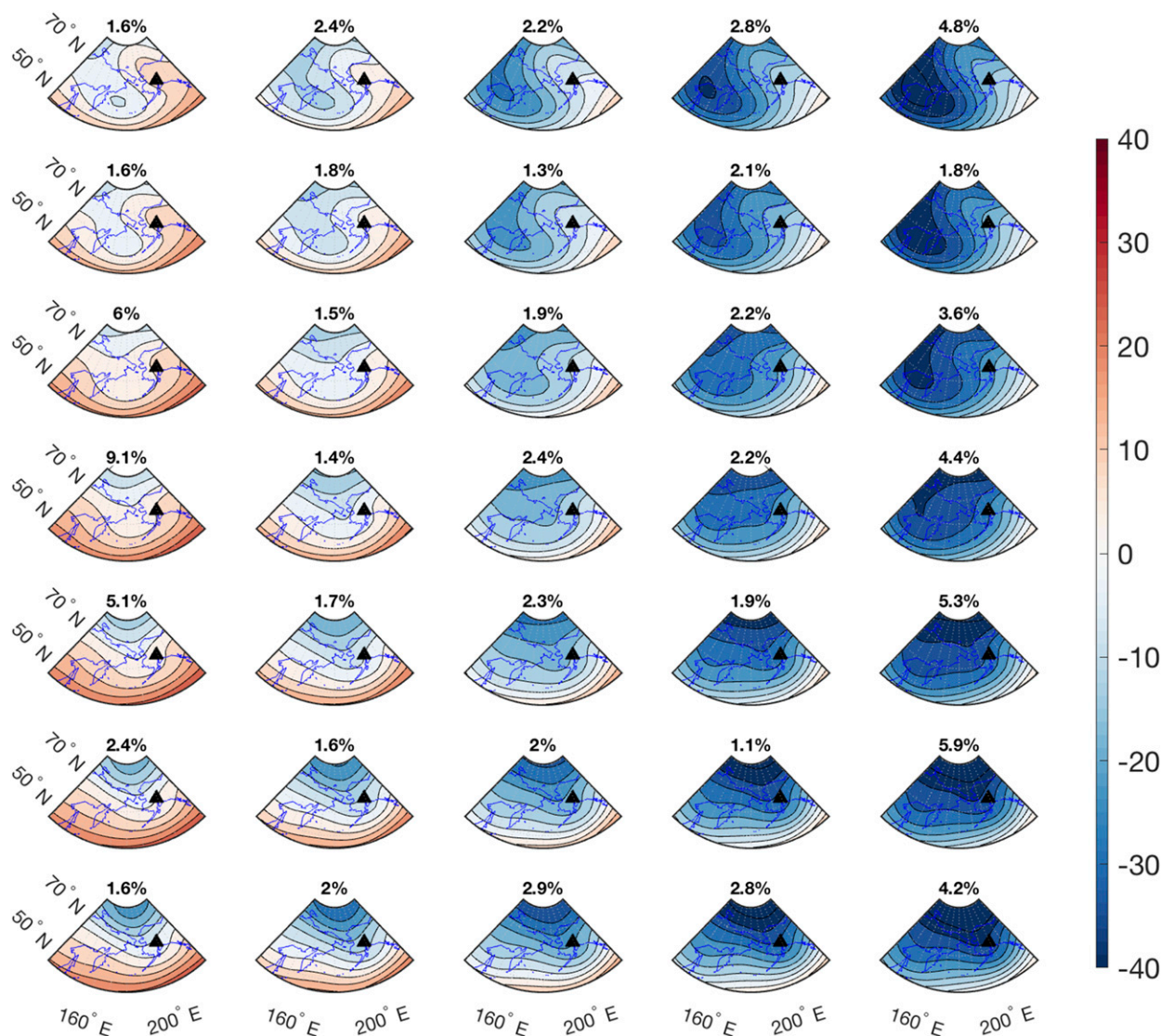


FIG. 7.  $7 \times 5$  SOM for 500 hPa GPH anomalies (dam), 1948–2018, 6-hourly reanalysis data. The black triangle marks the location of Denali. Isobars are in intervals of 5 dam. Percentage values above the SOM nodes indicate the percentage of input data points mapped to each node.

pattern—shows a decreasing frequency of occurrence (longest significant trend:  $-0.2$  occurrences/season for the 1955–2017 subperiod), while node (3, 2) has been occurring more often in some of the more recent subperiods (longest significant trend:  $+0.7$  occurrences/season for the 1983–2011 subperiod). In terms of dominant patterns, SOM results for high-wind days are relatively similar whether or not the input data are limited to the months of the climbing season, although the range of GPH anomalies is greater when taking into account the entire year (see the online supplemental material).

Analogous to Fig. 11, Fig. 12 shows a  $3 \times 2$  SOM for days during the climbing season in which wind speed is

below  $10 \text{ m s}^{-1}$ . Broadly speaking, the most frequent “low-wind” pattern [39% of input data mapped to node (1, 1) in Fig. 12] is similar to node (1, 1) in Fig. 9 and shows the characteristic summer-type GPH distribution of ridging over Alaska and a closed low in the Bering Sea. However, the low-wind version of this pattern is distinguished by a pronounced negative tilt of the ridge in the east, an extension of the low pressure area into the Gulf of Alaska, and a weak easterly flow over Denali. 30% of the input data are mapped to the “opposite” node (3, 2), which shows winter-type characteristics in the sense that GPH anomalies are largely negative and the pattern is more zonal. However, as in all the other low-wind nodes, the flow over Denali is

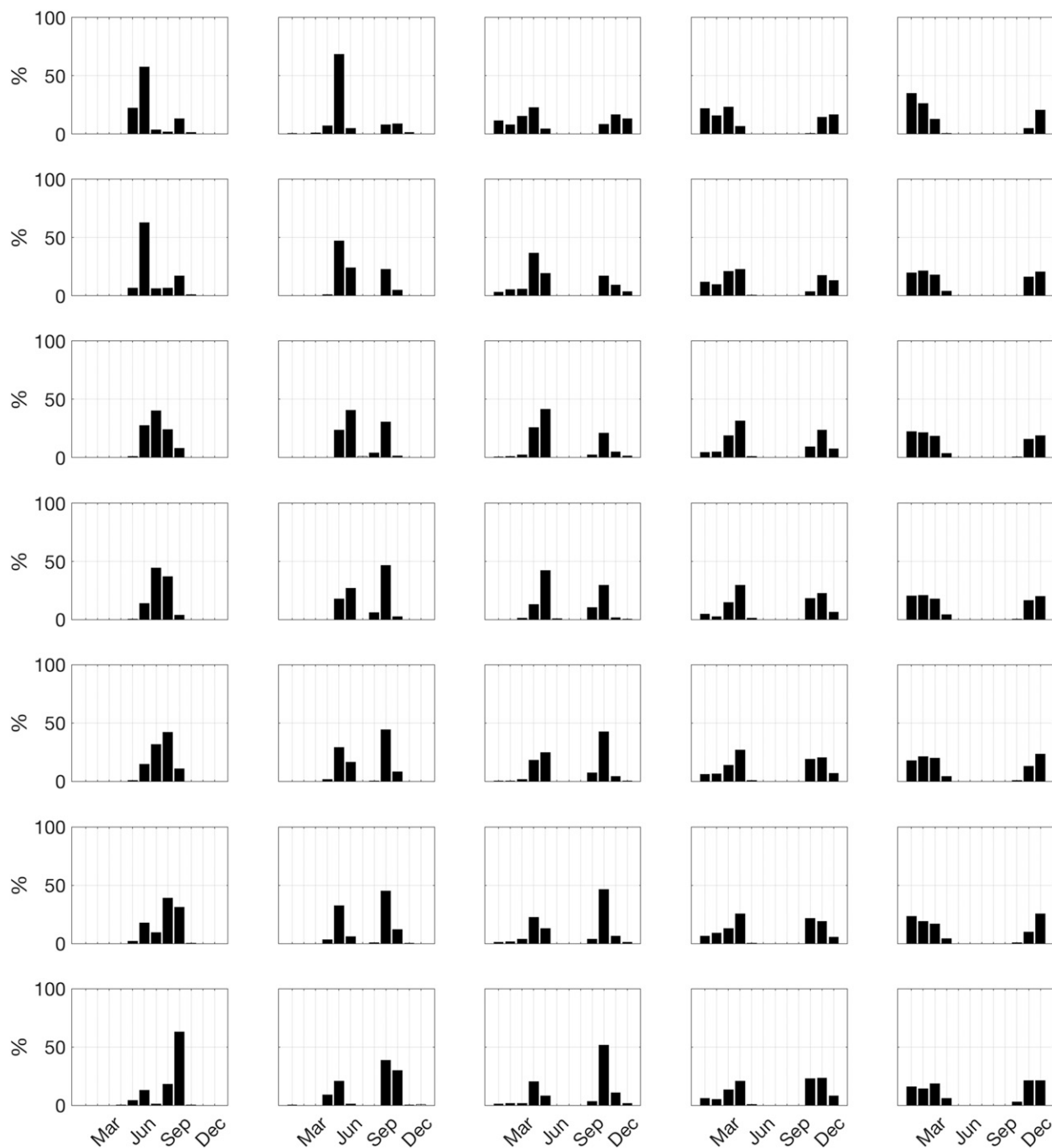


FIG. 8. The subplots correspond to the  $7 \times 5$  matrix of nodes in Fig. 7 and show the distribution of input data mapped to each node throughout the 12 months of the year.

comparatively weak and has a pronounced easterly component between a closed low in the Gulf of Alaska and the western most extension of the ridging over continental Alaska and western Canada, which together form the components of a high-over-low Rex block. As might be expected, the summer-type nodes in Fig. 12 occur mostly during the later half of the

climbing season, while the winter-type patterns occur earlier in the season, in April and May. A  $(3 \times 2)$  SOM of low-wind days for the entire year (see the online supplemental material), as opposed to the four months of the climbing season, shows a greater range of GPH anomalies between the nodes but is similar to Fig. 12 in terms of a weak, easterly flow over Denali, low pressure



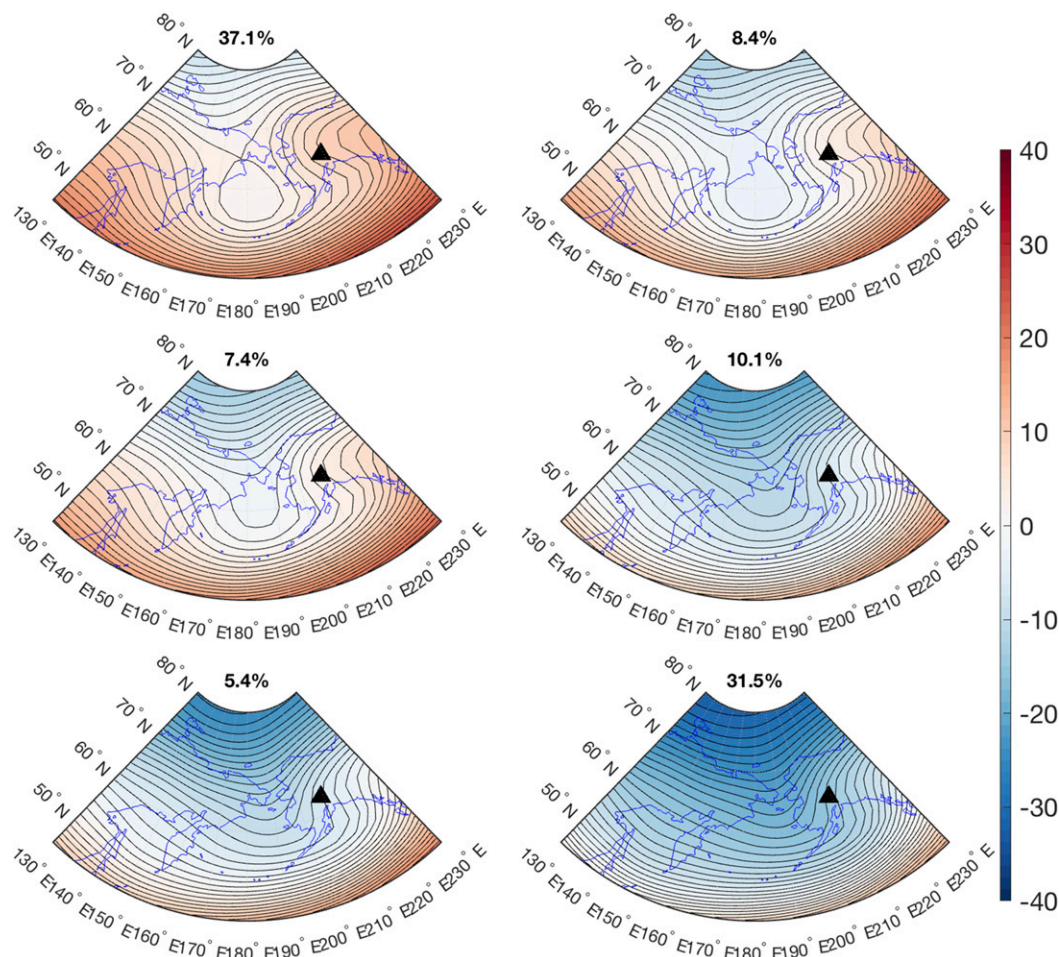


FIG. 9.  $3 \times 2$  SOM for 500 hPa GPH anomalies (dam) during the main climbing season (April–July). The black triangle marks the location of Denali. Isobars are in intervals of 1 dam. Percentage values above the SOM nodes indicate the percentage of input data points mapped to each node.

in the Gulf of Alaska, and a negative tilt to the axis of the ridge in the east.

#### 4. Discussion

The geographic isolation of Denali likely reduces the influence of regional surface topography on local conditions compared to less isolated mountains and the free atmosphere circulation of the 500 hPa reanalysis data may therefore serve as a useful approximation of conditions in the Denali summit region. However, the reanalysis data clearly have limitations in terms of temporal and spatial resolution of the on-mountain conditions relevant to climbers. Surface wind speed and direction on the main climbing route, and particularly in the Denali Pass area, likely differ significantly from reanalysis data, for example, due to local funneling effects. Furthermore, gusts—arguably of far greater importance to climbers’

safety than average winds—are not captured in the 6-hourly reanalysis wind speeds.

From a climatological point of view, the chances for “good” climbing weather with low wind speeds and relatively warm air temperatures are highest during the first half of July. However, these are not the only factors indicative of suitable climbing conditions and earlier months may be preferable in terms of reduced convective instability as well as snow conditions. Additionally, stormy synoptic patterns associated with high wind speeds occur throughout the year and in all months of the main climbing season. Climatological averages can only give a broad overview of the range of likely conditions throughout the seasons. For practical climbing purposes, short-term synoptic variability is the decisive factor.

Increasing trends in 500 hPa air temperature anomalies and GPH at the Denali grid cell, as well as a decrease



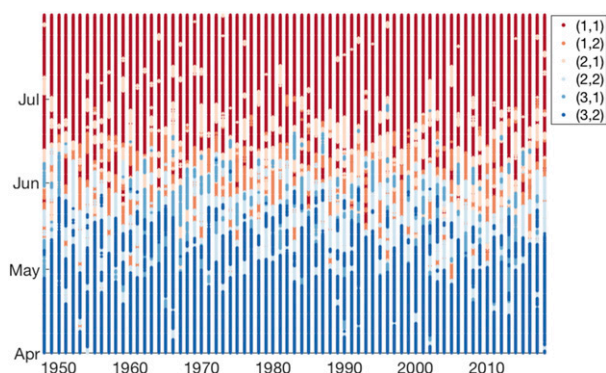


FIG. 10. Different colored markers correspond to the nodes in the  $3 \times 2$  SOM in Fig. 9 as indicated in the legend. The date and time of each node occurrence during the climbing season (vertical axis) is plotted against the respective year (horizontal axis) for the 1948–2018 reanalysis dataset.

in the number of very cold days during the climbing season, tie into observational evidence from other mountainous areas that suggests that higher elevations are not only warming, they may be warming at a faster rate than other regions (Auer et al. 2007; Gobiet et al. 2014; Rangwala and Miller 2012; Pepin et al. 2015). Winski et al. (2018) found that significant warming has occurred at high elevations in the Alaska Range during the last century, with a summer warming trend of at least  $1.92^\circ \pm 0.31^\circ\text{C}$  per century at Mount Hunter, which exceeds the warming observed at many low elevation locations in Alaska. While increasing air temperatures might have an overall positive effect on the cold-related dangers that climbers on Denali face, they may also lead to a deterioration of snow and ice conditions on the route and greater variability of the overall climbing conditions.

We use the SOM algorithm primarily to visualize recurring synoptic patterns in and upstream of the Denali region. The size of the SOM—that is, the number of nodes the input data are mapped to—determines the level of detail that can be seen in the variations of anomaly magnitudes and spatial distribution. In choosing a  $7 \times 5$  SOM for the primary analysis in Fig. 7 we followed a number of previous climatological studies, which found that a 35 node SOM shows the distribution of synoptic-scale circulation patterns at a resolution suitable for further analysis (Cassano and Cassano 2010; Hewitson and Crane 2002; Cassano et al. 2006; Lynch et al. 2006).

The  $7 \times 5$  SOM clearly reflects the seasonality of the location of the polar front. In the winter months, negative GPH anomalies dominate the northern Pacific subregion and the polar front and polar jet tend to pass over comparatively low latitudes. In the spring and early

summer, the polar vortex disintegrates, the polar front moves north, and the polar jet becomes weaker overall, leading to more meridional circulation patterns and weaker GPH gradients across the region.

The smaller  $3 \times 2$  SOM in Figs. 9, 11, and 12 obscure some of the details that a larger SOM can provide, but allow a broader clustering and a greater level of generalization. The nodes are placed throughout the distribution of the input data space such that the SOM in Fig. 9 effectively clusters the synoptic patterns of the climbing season into three types: a winter regime with a predominance of negative GPH anomalies in the region characterized by a relatively zonal flow; a summer regime with weaker GPH gradients, more positive GPH anomalies overall, and a higher-amplitude trough/ridge pattern; and a range of transitional patterns that fall between the winter and summer regimes. Patterns associated with high wind speeds in the Denali grid cell (Fig. 11) show a similar synoptic spectrum ranging from a more zonal circulation pattern associated with a strong polar jet to a higher-amplitude trough or closed low over the Bering Sea. The key characteristic these “windy” synoptic patterns have in common is a pronounced GPH gradient across Denali, resulting from either proximity to the polar jet or cyclogenesis in the Bering Sea paired with ridging over Interior Alaska. In contrast, calmer conditions tend to occur when low pressure in the Gulf of Alaska combines with a pronounced negative tilt of the ridge over Interior Alaska to produce a Rex-block-like pattern with a weak GPH gradient over Denali (Fig. 12).

The SOM results and trend analysis for the climbing season indicate that synoptic conditions associated with the winter regime may be occurring less often during recent decades, while the frequency of occurrence of summer-type patterns appears to be increasing. This could be explained by a shift toward earlier disintegration of the polar vortex in spring (which might cause an earlier switch to “summer regime” type synoptic patterns during the climbing season), an overall decrease of circulation patterns characterized by zonal flow related to rapid Arctic warming as identified by Francis and Vavrus (2015), or a combination thereof. It should be noted that any attempts at attribution of trends in node occurrence to large-scale climatic changes are speculative at best. Modeling results indicate a linkage between Arctic sea ice decline and the strength of the stratospheric polar vortex, with low sea ice cover during the early winter being tied to a weakening of the stratospheric polar vortex in midwinter (Kim et al. 2014). However, the dynamic coupling of stratospheric and

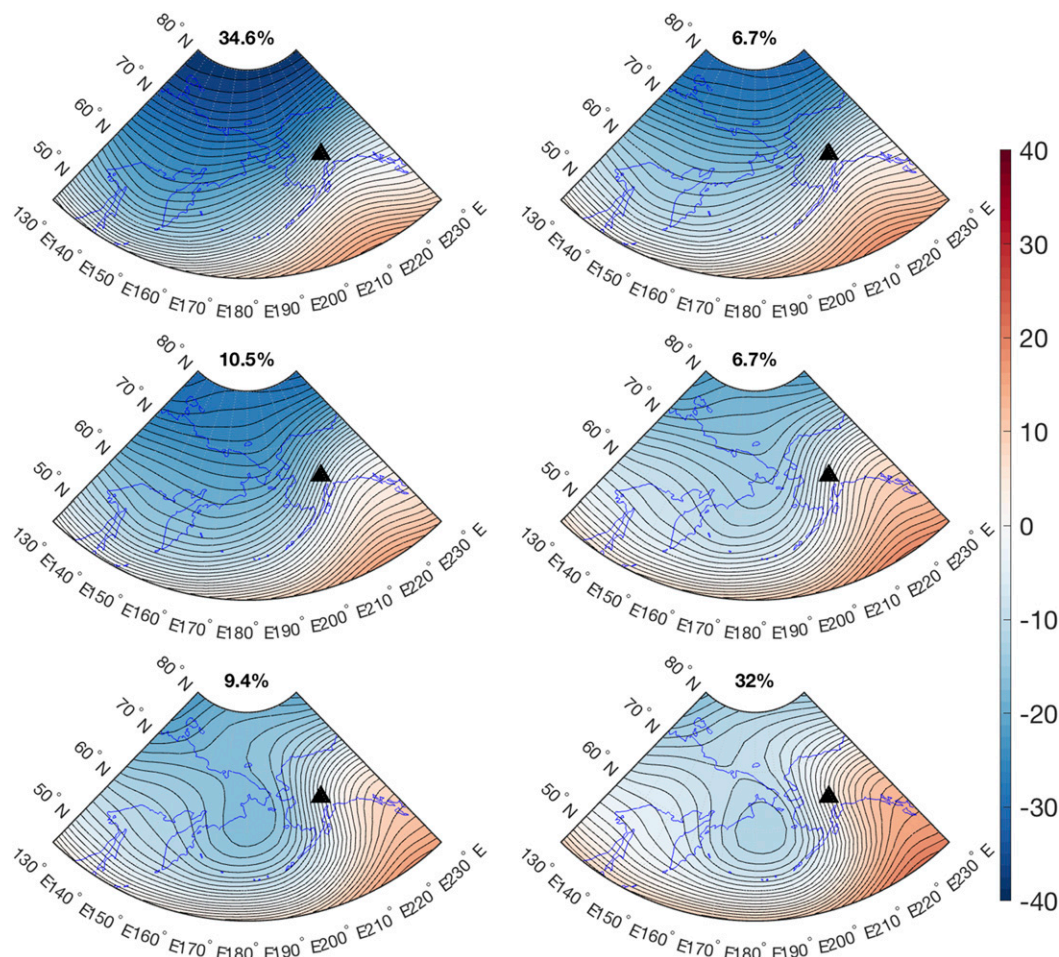


FIG. 11.  $3 \times 2$  SOM for 500 hPa GPH anomalies (dam) of the 1055 days on which wind speed was greater or equal to  $20 \text{ m s}^{-1}$  during the main climbing season (April–July), 1948–2018. The black triangle marks the location of Denali. Isobars are in intervals of 1 dam. Percentage values above the SOM nodes indicate the percentage of input data points mapped to each node.

tropospheric circulation is complex and incompletely understood (e.g., [Limpasuvan et al. 2005](#); [Douville 2009](#)), and significant uncertainties remain regarding the future development of large-scale circulation patterns such as the polar jet and the polar front ([Hartmann et al. 2013](#)).

## 5. Conclusions

The NCEP–NCAR reanalysis dataset 1 provides an overview of the range of conditions that can be expected in the summit regions of Denali throughout the year: From November to March, mean monthly air temperatures fall below  $-30^\circ\text{C}$  and synoptic patterns characterized by high wind speeds and negative GPH anomalies dominate the Denali region. In the spring and summer months, as the polar front moves north, positive GPH anomalies, higher temperatures, and

lower wind speeds occur more frequently. Nonetheless, synoptic patterns with extreme wind speeds unfavorable for climbing occur in all seasons. High-wind conditions are associated mainly with the polar jet passing directly over Denali, or cyclogenesis in the Bering Sea.

Reanalysis air temperatures at the 500 hPa level for the Denali grid cell were found to be increasing in concurrence with other studies. The number of very windy days ( $\geq 20 \text{ m s}^{-1}$ ) during the main climbing season shows a decreasing trend during the majority of the time series. The SOM analysis of the 1948–2018 reanalysis dataset indicates that the frequency of occurrence of certain weather patterns over Denali during the main climbing season (April–July) may be shifting toward more meridional, “summer type” patterns and fewer strongly zonal patterns with very low GPH anomalies.

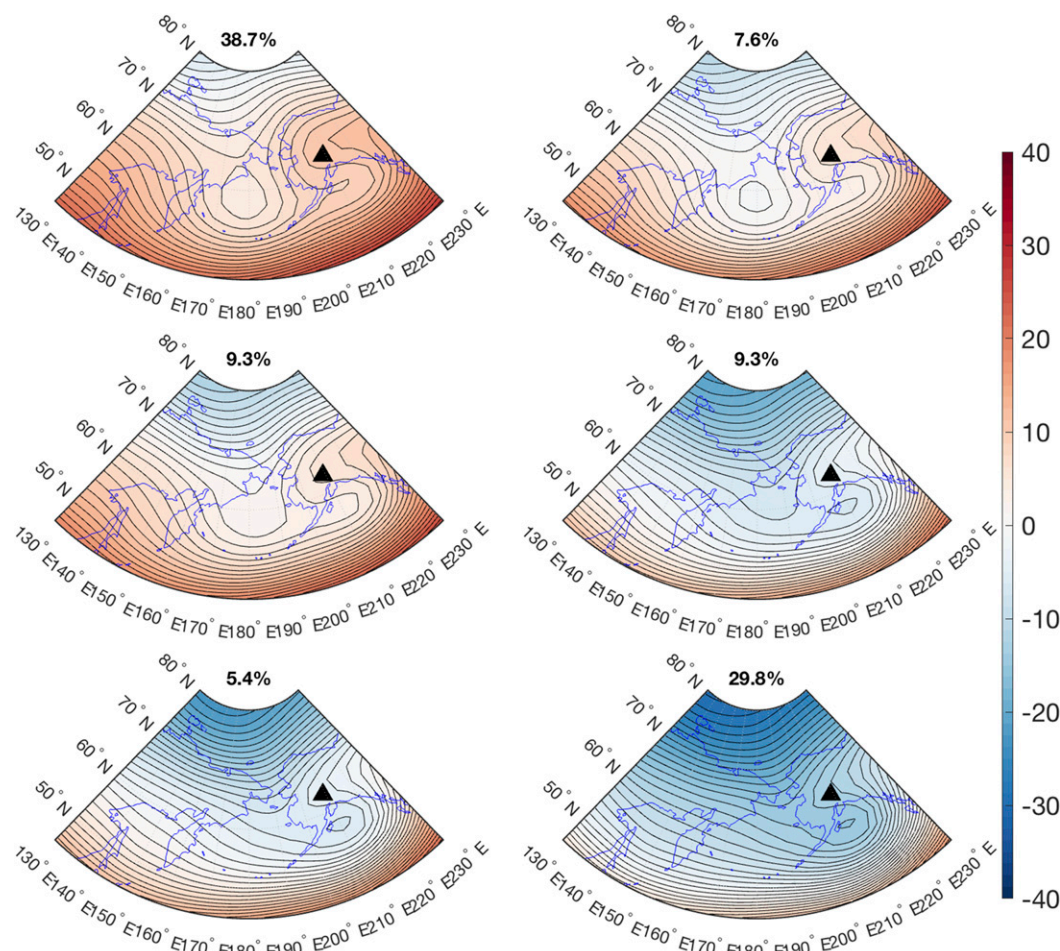


FIG. 12.  $3 \times 2$  SOM for 500 hPa GPH anomalies (dam) of the 3545 days on which wind speed was less than  $10 \text{ m s}^{-1}$  during the main climbing season (April–July), 1948–2018. The black triangle marks the location of Denali. Isobars are in intervals of 1 dam. Percentage values above the SOM nodes indicate the percentage of input data points mapped to each node.

**Acknowledgments.** This study was supported by the Alaska Climate Research Center at the Geophysical Institute of the University of Alaska Fairbanks.

#### REFERENCES

- Auer, I., and Coauthors, 2007: HISTALP—Historical instrumental climatological surface time series of the Greater Alpine Region. *Int. J. Climatol.*, **27**, 17–46, <https://doi.org/10.1002/joc.1377>.
- Businger, S., and R. J. Reed, 1989: Cyclogenesis in cold air masses. *Wea. Forecasting*, **4**, 133–156, [https://doi.org/10.1175/1520-0434\(1989\)004<0133:CICAM>2.0.CO;2](https://doi.org/10.1175/1520-0434(1989)004<0133:CICAM>2.0.CO;2).
- Cassano, E., and J. Cassano, 2010: Synoptic forcing of precipitation in the Mackenzie and Yukon River basins. *Int. J. Climatol.*, **30**, 658–674, <https://doi.org/10.1002/JOC.1926>.
- Cassano, J. J., P. Uotila, and A. Lynch, 2006: Changes in synoptic weather patterns in the polar regions in the twentieth and twenty-first centuries, part I: Arctic. *Int. J. Climatol.*, **26**, 1027–1049, <https://doi.org/10.1002/joc.1306>.
- Denali National Park Service, 2018: Annual mountaineering summaries. Accessed 13 February 2019, <https://www.nps.gov/dena/planyourvisit/mountaineering-summary-reports.htm>.
- Douville, H., 2009: Stratospheric polar vortex influence on Northern Hemisphere winter climate variability. *Geophys. Res. Lett.*, **36**, L18703, <https://doi.org/10.1029/2009GL039334>.
- Francis, J. A., and S. J. Vavrus, 2015: Evidence for a wavier jet stream in response to rapid Arctic warming. *Environ. Res. Lett.*, **10**, 014005, <https://doi.org/10.1088/1748-9326/10/1/014005>.
- Gobiet, A., S. Kotlarski, M. Beniston, G. Heinrich, J. Rajczak, and M. Stoffel, 2014: 21st century climate change in the European Alps—A review. *Sci. Total Environ.*, **493**, 1138–1151, <https://doi.org/10.1016/j.scitotenv.2013.07.050>.
- Hartmann, B., and G. Wendler, 2005: The significance of the 1976 Pacific climate shift in the climatology of Alaska. *J. Climate*, **18**, 4824–4839, <https://doi.org/10.1175/JCLI3532.1>.
- Hartmann, D. L., and Coauthors, 2013: Observations: Atmosphere and surface. *Climate Change 2013: The Physical Science Basis*, T. F. Stocker et al., Eds., Cambridge University Press, 159–254.



- Hewitson, B. C., and R. G. Crane, 2002: Self-organizing maps: Applications to synoptic climatology. *Climate Res.*, **22**, 13–26, <https://doi.org/10.3354/cr022013>.
- Hu, D., Z. Guan, W. Tian, and R. Ren, 2018: Recent strengthening of the stratospheric Arctic vortex response to warming in the central North Pacific. *Nat. Commun.*, **9**, 1697, <https://doi.org/10.1038/s41467-018-04138-3>.
- Kalnay, E., and Coauthors, 1996: The NCEP/NCAR 40-Year Reanalysis Project. *Bull. Amer. Meteor. Soc.*, **77**, 437–471, [https://doi.org/10.1175/1520-0477\(1996\)077<0437:TNYRP>2.0.CO;2](https://doi.org/10.1175/1520-0477(1996)077<0437:TNYRP>2.0.CO;2).
- Kendall, M. G., 1955: *Rank Correlation Methods*. 2nd ed. Griffin, 195 pp.
- Kim, B. M., S. W. Son, S. K. Min, J. H. Jeong, S. J. Kim, X. Zhang, T. Shim, and J. H. Yoon, 2014: Weakening of the stratospheric polar vortex by Arctic sea-ice loss. *Nat. Commun.*, **5**, 4646, <https://doi.org/10.1038/ncomms5646>.
- Kohonen, T., 1989: *Self-Organization and Associative Memory*. 3rd ed. Springer-Verlag, 312 pp.
- , 1990: The self-organizing map. *Proc. IEEE*, **78**, 1464–1480, <https://doi.org/10.1109/5.58325>.
- , 1991: Self-organizing maps: Optimization approaches. *Proc. Int. Conf. on Artificial Neural Networks*, Espoo, Finland, European Neural Network Society, 981–990.
- , 2001: *Self-Organizing Maps*. Springer, 501 pp.
- Limpasuvan, V., D. L. Hartmann, D. W. Thompson, K. Jeev, and Y. L. Yung, 2005: Stratosphere-troposphere evolution during polar vortex intensification. *J. Geophys. Res.*, **110**, D24101, <https://doi.org/10.1029/2005JD006302>.
- Liu, Y., and R. H. Weisberg, 2011: A review of self-organizing map applications in meteorology and oceanography. *Self Organizing Maps—Applications and Novel Algorithm Design*, J. I. Mwasiagi, Ed., IntechOpen, 253–272.
- Lynch, A., Uotila, P., Cassano, J. J., 2006: Changes in synoptic weather patterns in the polar regions in the twentieth and twenty-first centuries, part 2: Antarctic. *Int. J. Climatol.*, **26**, 1181–1199, <https://doi.org/10.1002/JOC.1305>.
- Mann, H. B., 1945: Nonparametric tests against trends. *Econometrica*, **13**, 245–259, <https://doi.org/10.2307/1907187>.
- Marcus, S. L., O. de Viron, and J. O. Dickey, 2011: Abrupt atmospheric torque changes and their role in the 1976–1977 climate regime shift. *J. Geophys. Res.*, **116**, D03107, <https://doi.org/10.1029/2010JD015032>.
- McIntosh, S. E., A. D. Campbell, J. Dow, and C. K. Grissom, 2008: Mountaineering fatalities on Denali. *High Alt. Med. Biol.*, **9**, 89–95, <https://doi.org/10.1089/ham.2008.1047>.
- , A. Brillhart, J. Dow, and C. K. Grissom, 2010: Search and rescue activity on Denali, 1990 to 2008. *Wilderness Environ. Med.*, **21**, 103–108, <https://doi.org/10.1016/j.wem.2009.12.024>.
- , A. Campbell, D. Weber, J. Dow, E. Joy, and C. K. Grissom, 2012: Mountaineering medical events and trauma on Denali, 1992–2011. *High Alt. Med. Biol.*, **13**, 275–280, <https://doi.org/10.1089/ham.2012.1027>.
- Olefs, M., A. Fischer, and J. Lang, 2010: Boundary conditions for artificial snow production in the Austrian Alps. *J. Appl. Meteor. Climatol.*, **49**, 1096–1113, <https://doi.org/10.1175/2010JAMC2251.1>.
- Osterberg, E. C., and Coauthors, 2017: The 1200 year composite ice core record of Aleutian low intensification. *Geophys. Res. Lett.*, **44**, 7447–7454, <https://doi.org/10.1002/2017GL073697>.
- Overland, J. E., J. M. Adams, and N. A. Bond, 1999: Decadal variability of the Aleutian low and its relation to high-latitude circulation. *J. Climate*, **12**, 1542–1548, [https://doi.org/10.1175/1520-0442\(1999\)012<1542:DVOTAL>2.0.CO;2](https://doi.org/10.1175/1520-0442(1999)012<1542:DVOTAL>2.0.CO;2).
- Pepin, N., and Coauthors, 2015: Elevation-dependent warming in mountain regions of the world. *Nat. Climate Change*, **5**, 424–430, <https://doi.org/10.1038/nclimate2563>.
- Pickart, R. S., A. M. Macdonald, G. W. K. Moore, I. A. Renfrew, J. E. Walsh, and W. S. Kessler, 2009: Seasonal evolution of Aleutian low pressure systems: Implications for the North Pacific subpolar circulation. *J. Phys. Oceanogr.*, **39**, 1317–1339, <https://doi.org/10.1175/2008JPO3891.1>.
- Rangwala, I., and J. R. Miller, 2012: Climate change in mountains: A review of elevation-dependent warming and its possible causes. *Climatic Change*, **114**, 527–547, <https://doi.org/10.1007/s10584-012-0419-3>.
- Rodionov, S. N., J. E. Overland, and N. A. Bond, 2005a: The Aleutian low and winter climatic conditions in the Bering Sea. Part I: Classification. *J. Climate*, **18**, 160–177, <https://doi.org/10.1175/JCLI3253.1>.
- , —, and —, 2005b: Spatial and temporal variability of the Aleutian climate. *Fish. Oceanogr.*, **14**, 3–21, <https://doi.org/10.1111/j.1365-2419.2005.00363.x>.
- , N. A. Bond, and J. E. Overland, 2007: The Aleutian low, storm tracks, and winter climate variability in the Bering Sea. *Deep-Sea Res. II*, **54**, 2560–2577, <https://doi.org/10.1016/j.dsr2.2007.08.002>.
- Serreze, M. C., F. Carse, R. G. Barry, and J. C. Rogers, 1997: Icelandic low cyclone activity: Climatological features, linkages with the NAO, and relationships with recent changes in the Northern Hemisphere circulation. *J. Climate*, **10**, 453–464, [https://doi.org/10.1175/1520-0442\(1997\)010<0453:ILCACF>2.0.CO;2](https://doi.org/10.1175/1520-0442(1997)010<0453:ILCACF>2.0.CO;2).
- Sheridan, S. C., and C. C. Lee, 2011: The self-organizing map in synoptic climatological research. *Prog. Phys. Geogr.*, **35**, 109–119, <https://doi.org/10.1177/0309133310397582>.
- Sugimoto, S., and K. Hanawa, 2009: Decadal and interdecadal variations of the Aleutian low activity and their relation to upper oceanic variations over the North Pacific. *J. Meteor. Soc. Japan*, **87**, 601–614, <https://doi.org/10.2151/JMSJ.87.601>.
- Sun, J., and B. Tan, 2013: Mechanism of the wintertime Aleutian low–Icelandic low seesaw. *Geophys. Res. Lett.*, **40**, 4103–4108, <https://doi.org/10.1002/grl.50770>.
- Vesanto, J., J. Himberg, E. Alhoniemi, and J. Parhankangas, 1999: Self-organizing map in Matlab: The SOM Toolbox. *Proc. Matlab DSP Conf.*, Vol. 99, Espoo, Finland, 35–40.
- Wang, P., J. X. Wang, H. Zhi, Y. Wang, and X. Sun, 2012: Circulation indices of the Aleutian low pressure system: Definitions and relationships to climate anomalies in the Northern Hemisphere. *Adv. Atmos. Sci.*, **29**, 1111–1118, <https://doi.org/10.1007/s00376-012-1196-7>.
- Winski, D., and Coauthors, 2017: Industrial-age doubling of snow accumulation in the Alaska Range linked to tropical ocean warming. *Sci. Rep.*, **7**, 17869, <https://doi.org/10.1038/s41598-017-18022-5>.
- , and Coauthors, 2018: A 400-year ice core melt layer record of summertime warming in the Alaska Range. *J. Geophys. Res. Atmos.*, **123**, 3594–3611, <https://doi.org/10.1002/2017JD027539>.
- Zhu, X., J. Sun, Z. Liu, Q. Liu, and J. E. Martin, 2007: A synoptic analysis of the interannual variability of winter cyclone activity in the Aleutian low region. *J. Climate*, **20**, 1523–1538, <https://doi.org/10.1175/JCLI4077.1>.